INTERNATIONAL JOURNAL OF
Minerals, Metallurgy and Materials

Volume 31, Number 8, August 2024
Page 1876

Research Article https://doi.org/10.1007/s12613-023-2779-2

Evolution of microstructure and properties of a novel Ni-based superalloy during stress relief annealing

Lei Jia[1)], *Heng Cui*[1),✉], *Shufeng Yang*[2),✉], *Shaomin Lü*[3,4)], *Xingfei Xie*[3,4)], *and Jinglong Qu*[3,4)]

1) Collaborative Innovation Center of Steel Technology, University of Science and Technology Beijing, Beijing 100083, China
2) State Key Laboratory of Advanced Metallurgy, University of Science and Technology Beijing, Beijing 100083, China
3) Beijing GAONA Materials & Technology Co., Ltd., Beijing 100081, China
4) High-Temperature Materials Institute, Central Iron and Steel Research Institute, Beijing 100081, China
(Received: 28 August 2023; revised: 1 November 2023; accepted: 6 November 2023)

Abstract: We discussed the decrease in residual stress, precipitation evolution, and mechanical properties of GH4151 alloy in different annealing temperatures, which were studied by the scanning electron microscope (SEM), high-resolution transmission electron microscopy (HRTEM), and electron backscatter diffraction (EBSD). The findings reveal that annealing processing has a significant impact on diminishing residual stresses. As the annealing temperature rose from 950 to 1150°C, the majority of the residual stresses were relieved from 60.1 MPa down to 10.9 MPa. Moreover, the stress relaxation mechanism transitioned from being mainly controlled by dislocation slip to a combination of dislocation slip and grain boundary migration. Meanwhile, the annealing treatment promotes the decomposition of the Laves, accompanied by the precipitation of μ-(Mo_6Co_7) starting at 950°C and reaching a maximum value at 1050°C. The tensile strength and plasticity of the annealing alloy at 1150°C reached the maximum (1394 MPa, 56.1%) which was 131%, 200% fold than those of the as-cast alloy (1060 MPa, 26.6%), but the oxidation process in the alloy was accelerated at 1150°C. The enhancement in durability and flexibility is primarily due to the dissolution of the brittle phase, along with the shape and dispersal of the γ′ phase.

Keywords: GH4151 alloy; annealing treatment; residual stress; precipitation evolution; strength; mechanical properties

1. Introduction

As advancements in aerospace technology continue, bigger and more efficient aero-engines with a higher thrust weight ratio are being developed [1–2]. Nickel-based superalloys are commonly chosen for their exceptional mechanical characteristics and the capability to resist oxidation even under extreme temperatures [3–5]. The GH4151 alloy, a newly developed high-alloy γ–γ′ nickel-based superalloy, is a cast and wrought (C&W) superalloy designed for use in turbine disks that can function up to 800°C [6]. This particular alloy comprises more than 34wt% solution-strengthening elements such as W, Mo, Cr, and Co, and over 10wt% age-precipitation strengthening elements like Al, Ti, and Nb [7]. Ultimately, the γ′ phase forms up to 55% of the mass fraction at equilibrium [8–9], rendering the GH4151 alloy's smelting difficulty nearly at the deformed superalloys' highest limit [10].

At present, the deformed superalloys are prepared by two-component processes (vacuum induction melting (VIM) + vacuum arc remelting (VAR) or VIM + electroslag remelting (ESR)) or three-component processes (VIM + ESR + VAR) [3]. In the actual production process, GH4151 contains a large amount of age-hardening (Mo, Cr, W) and precipitation-strengthening elements (Al, Ti, Nb), resulting in poor thermoplasticity of the alloy and obvious cracks in the electrodes of the alloy prepared by VIM [11–12]. Regrettably, hot cracking is a common issue in large-scale superalloy VIM ingots, which leads to varying technological parameters such as electric current and voltage in subsequent processes like electro-slag remelting or vacuum arc remelting [13].

Hot cracking is a significant flaw in metallurgical procedures [14]. Evidently, it takes place in the final phase of solidification [15] and is triggered by (i) the broad freezing scope due to considerable alloying [16–17], (ii) the emergence of diverse phases such as γ/γ′ eutectics [18–19] and Laves [9,20], (iii) inadequate liquid supply in the semi-solid stage [21], and (iv) the excessive tensile residual stress [22] and depleted ductility [23] resulting from the rapid γ′ precipitation in the VIM process.

The casting parameters and chemical compositions are difficult to change under the current industrial processing settings [24]. However, eliminating residual stresses during the solidification and cooling process through annealing treatment is an effective way to solve the cracking of VIM electrodes [25–26]. Ding *et al.* [27] studied the formation of residual stress in Inconel 738LC alloy at different annealing

✉ Corresponding authors: Heng Cui E-mail: cuiheng@ustb.edu.cn; Shufeng Yang E-mail: yangshufeng@ustb.edu.cn

temperatures. After annealing at 800°C, dislocation migration and grain boundary-type transformation occurred, forming short rod-like γ′ phase (240–440 nm). The type of grain boundary carbides changed from MC to $M_{23}C_6$, and the residual stress decreased from 380.94 to −66.7 MPa. Zhu *et al.* [28] conducted a study on the reduction of residual stress in forged bar Inconel 718 alloy that had been solid solution annealed with varying pretreatment. They noted that as the pretreatment temperature rose from 680 to 720°C, promoting the nucleation and precipitation of the γ″ phase, there was an increase in the rate of residual stress reduction from 52% to 65%. In the experiments on Inconel 738 conducted by Wang *et al.* [29], the most effective procedure was hot isostatic pressing (HIP) for 4 h at either 920 or 1175°C. This method resulted in a more uniform microstructure in terms of γ′ precipitation, thereby further enhancing its mechanical properties.

However, there have been limited studies on the evolution of the precipitation and minimizing initial residual stresses in the highly alloyed VIM electrode superalloys during the annealing process. This study explores the outcome of residual stress relaxation, the changes in precipitated phases, and the high-temperature tensile characteristics of the GH4151 alloy when subjected to a stress relief annealing process. Moreover, the combination of microscopy (scanning electron microscope (SEM), transmission electron microscopy (TEM), and electron backscatter diffraction (EBSD)) and mechanical properties tests were used to determine the contribution of the annealing process to the strength. It is expected that this study will guide for reducing and controlling residual stresses and optimizing the performance of VIM electrode superalloy parts.

2. Experimental

2.1. Materials

The ϕ280 mm GH4151 ingots were made using VIM, with the details of their chemical composition presented in Table 1. The annealing process was carried out in a BLMT-1600 tube furnace at temperatures of 950, 1050, and 1150°C, respectively, with the furnace heating up at a rate of 5°C/min, holding for 8 h, and then cooling to room temperature at 0.3°C/min. The types and temperatures of the precipitates in the GH4151 alloy were calculated by Thermo-Calc. The temperature range for the simulation is established between 200 and 1400°C, providing findings at every 10°C increment until a segment of the liquid reaches 2%. The as-cast and annealed samples at different temperatures were analyzed using X-ray diffraction spectroscopy (XRD, X-ray 6000 with Cu $K_{\alpha 1}$ radiation, $\lambda = 1.5405$ Å, scanning speed 10°/min). The results were calibrated by Search match.

Table 1. GH4151 alloy composition wt%

C	Al	Ti	Cr	Co	Nb	Mo	W	V	La	Ni
0.068	3.84	2.76	11.35	14.90	3.41	4.62	3.18	0.48	0.02	Bal.

2.2. Microstructure characterization

The fracture morphology of the tensile specimens in the different annealing temperatures was observed in a quanta 200 FEG scanning electron microscope. At the same time, the samples were electropolished using a solution of 20 mL H_2SO_4 + 80 mL CH_3OH at voltage range between 10 to 20 V for a duration of 10–15 s. The microscopic architectural designs of the annealed samples taken from various temperature points were studied through the use of EBSD with a stepping size of 6.5 μm. The scanning data acquired was later scrutinized and interpreted using the HKL-Channel 5 software application. The crystal structures of the precipitates between the dendrites were identified via TEM. The TEM specimens were created by slicing the samples into 500 μm thick pieces. The samples were mechanically ground to achieve a thickness of 60 μm and subsequently shaped into circular slices with a diameter of 3 mm. Afterward, twin-jet electro-polishing was employed, performed in a solution comprised of 10vol% $HClO_4$ and 90vol% CH_3CH_2OH at a temperature of 20°C and voltage of 24 V. The next stage involved conducting TEM examinations. For this, the Talos F200X G2 transmission electron microscope from Thermo Fisher, located in Waltham, MA, USA, was used. This device was operated at an acceleration voltage of 200 kV to perform the TEM tests.

2.3. Mechanical property analysis

The tensile strength of both the as-cast and annealed GH4151 alloy was measured using a Gleeble-3800 thermal simulation testing apparatus. The test was conducted at a temperature of 800°C, with a nominal strain rate of 0.1 s^{-1}. The dimensions of the sample were ϕ6 mm × 116 mm, with a gauge distance of 12 mm. A Vickers hardness tester (VH1102), applying a weight of 500 g for a duration of 15 s, was used to evaluate the hardness of the GH4151 alloys. To achieve averaged values, no less than ten measurements were carried out. Moreover, in view of the strong connection between the dynamic thermal stress and the ultimate residual stress, the Vickers micro-indentation technique was employed to examine the residual stress of the deposits [30]. The residual stresses (σ_{res}) and residual strains (ε_{res}) followed the following relationship.

$$\varepsilon_{res} = \left(\frac{H}{3K}\right)^{1/n} - 0.08 \tag{1}$$

$$\sigma_{res} = K|\varepsilon_{res}|^n \left[\exp\left(\frac{c^2-1}{0.32}\right) - 1\right] \tag{2}$$

where the K and n are material constants that can be obtained from the uniaxial stress–strain curve ($\sigma = K\varepsilon_p^n$, where σ is stress and ε_p is strain). H is the microhardness of the alloy, and the area ratio c^2 between the actual projected contact area A and the nominal projected contact area A_{nom} of the diamond

indentation is such that $c^2 = A/A_{nom}$. A diamond indentation's nominal projected contact area can be defined as $A_{nom} = [(L_1 + L_2)/2]^2/2$, where L_1 and L_2 are the diagonal lengths of the sharp indenter, seen Fig. 1.

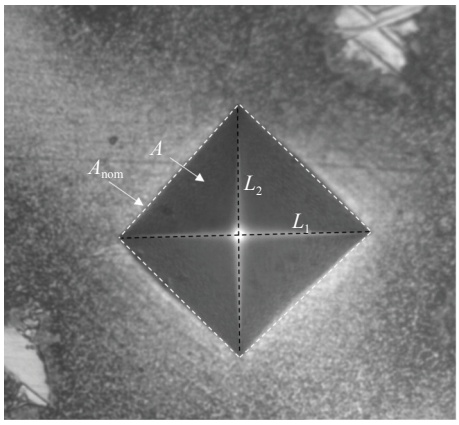

Fig. 1. Schematic diagram of induction-assisted as-cast equipment.

3. Results

3.1. Crack characterization

Fig. 2 depicts the large-scale structure of a VIM ingot, measuring 280 mm in diameter and 25 mm in thickness. From Fig. 2(a), it can be seen that a columnar grain region with a width of approximately 35 mm has formed at the ingot boundary, while an equiaxed grain region has formed within the ingot [31]. In addition, the cracks across the VIM ingot are the largest in the center of the ingot, reaching about 5 mm. This particular feature implies that the fissure originates from the core of the VIM ingot and gradually extends towards its outer parts. Fig. 2(b, c) presents the breakage structure of the ingot. The fracture surface reveals the dendritic framework morphology and evidence of oxidation, with an absence of any dimples. Such findings point towards hot tearing mechanisms [13,17]. In the meantime, Fig. 2(d) shows that the cracks extend along the grain boundaries, and these are consistent with brittle fracture characteristics. This can be attributed to the brittle precipitates such as Laves and ($\gamma + \gamma'$) in the interdendritic space when the temperature is below the solidus, as shown in Fig. 2(e). Furthermore, it is necessary to explore the impact of both the organization and the evolution of the precipitated phases on the mechanical characteristics during the annealing process.

3.2. Precipitation evolution

Fig. 3(a)–(d) shows high-magnification morphologies of the precipitation phase of as-cast and annealed samples at different temperatures. In the areas between the dendrites of the cast alloy (as shown in Fig. 3(a)), we can observe the precipitation of three distinct phases: a gray, sunflower-like phase indicated by the red arrow, a white, blocky phase highlighted by the white arrow, and a gray, angular phase denoted by the blue arrow. The elemental makeup of the precipitates was studied quantitatively using scanning electron microscope-energy dispersive spectroscopy (SEM-EDS), as shown in Table 2. For the phase that looks similar to a sunflower, the atomic ratio of Ni to the combined total of Al and Ti is roughly 3, exhibiting element properties akin to those of the γ' phase [32]. There exists a white and blocky phase (marked by white arrow) distributed on both sides of ($\gamma + \gamma'$) eutectic (Fig. 4(a)), enriched in Mo, Co, Cr, and Nb, and the the crystal structure is hexagonal possessing dimensions of a = 0.4901 nm and c = 0.7840 nm, c/a = 1.60, aligning with the characteristics of the Laves phase [33]. Additionally, the selected area diffraction (SAD) analysis shows that the sunflower-like phase's crystal structure shown in Fig. 4(b) is facet-centered cubic ($a \approx 0.346$ nm), suggesting it is a ($\gamma + \gamma'$)

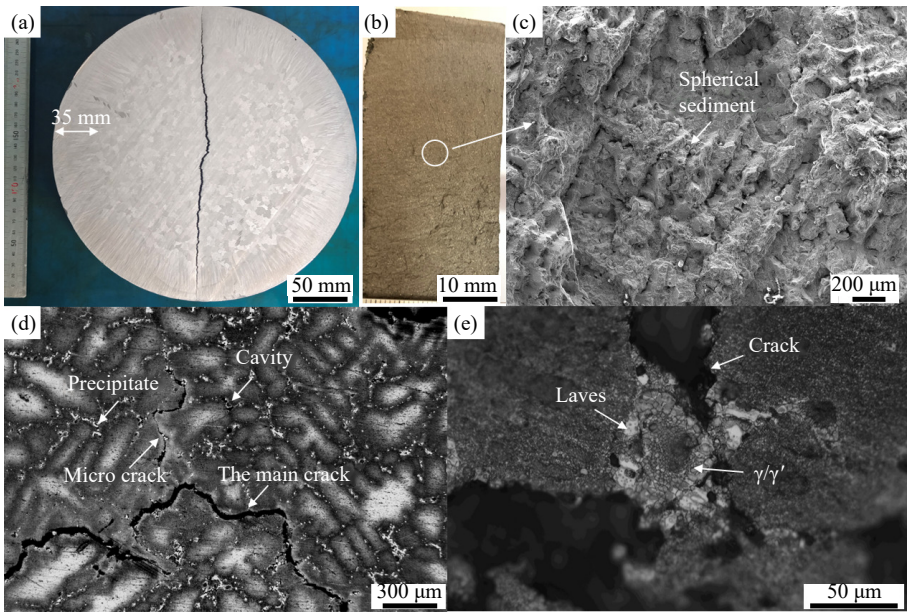

Fig. 2. (a) Fracture characteristics of ϕ280 mm VIM ingot; (b) fracture morphology; (c) fracture surface in smaller regions; (d) microstructure of cracks; (e) cracking in the vicinity precipitate phase of interdendritic.

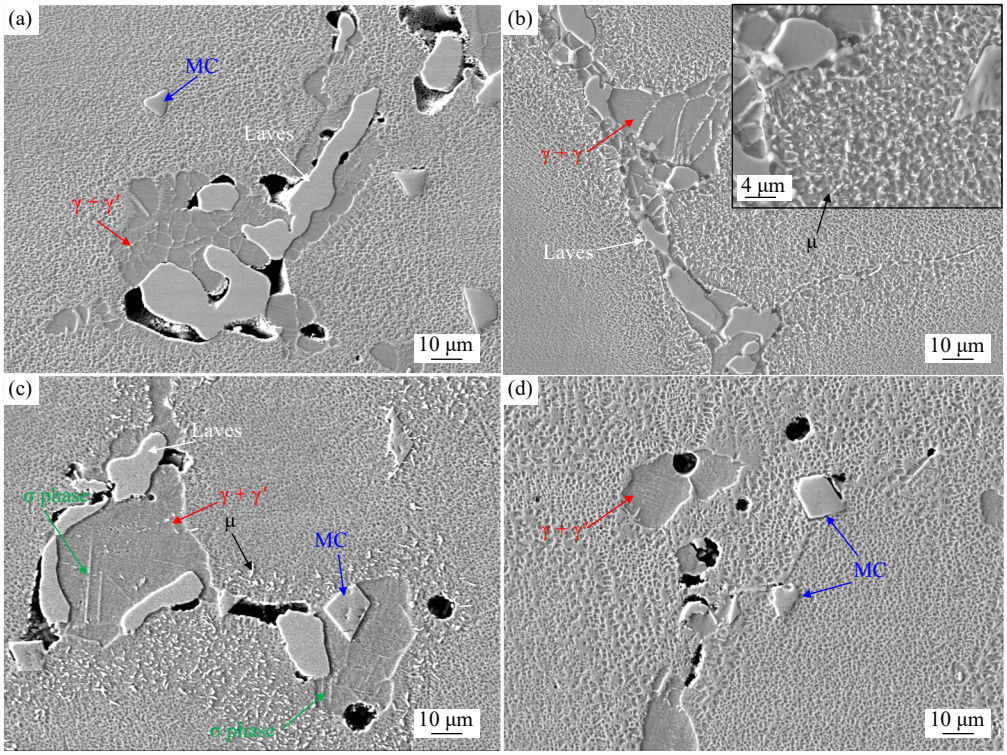

Fig. 3. (a) Precipitation phase morphologies of as-cast and annealed samples at different temperatures: (b) 950, (c) 1050, and (d) 1150°C. Inset in (b) shows a local magnified view of the μ phase.

Table 2. Compositions of precipitation phases measured by SEM-EDS and TEM-EDS at%

Presumed phase	Measure methods	C	Al	Ti	Cr	Co	Ni	Nb	Mo	W
γ + γ′	SEM-EDS		10.91	7.61	3.18	10.82	62.84	3.77	0.62	0.24
Laves	SEM-EDS		0.57	0.83	19.31	23.47	28.55	11.18	14.08	1.99
MC	TEM-EDS	48.21	0.00	16.81	0.39	0.39	1.74	29.82	1.91	0.73
μ	TEM-EDS		2.39	1.64	18.20	21.32	26.52	6.82	18.97	4.14
σ phase	TEM-EDS		3.42	3.92	10.38	15.28	51.95	3.36	9.04	2.64

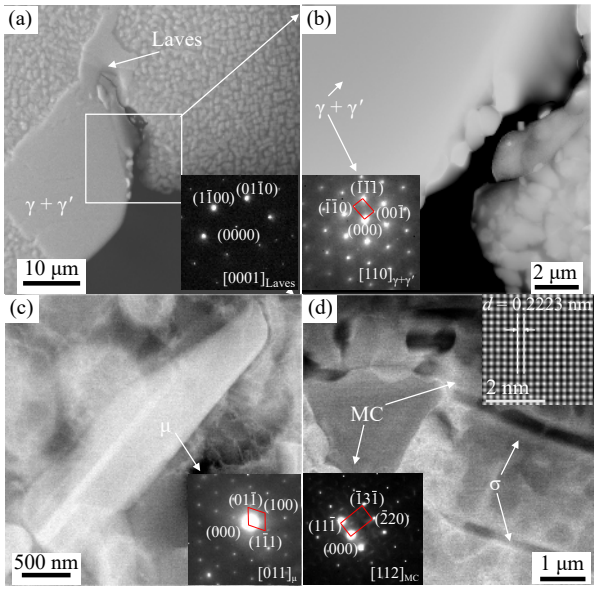

Fig. 4. TEM morphology and the relevant selected area diffraction patterns of the as-cast sample's precipitates and annealed at 1050°C: (a) Laves pahse; (b) γ + γ′; (c) μ phase; (d) MC phase.

eutectic phase.

With the annealing process, the morphology and type of precipitates changed. Once the temperature reaches 950 and 1050°C as illustrated in Fig. 3(b), the volume fraction of the Laves phase diminishes, and small, bright particles develop around the grain boundaries and Laves phase. Further analysis using TEM bright field imaging and SAD indicate that these bright particles exhibit a hexagonal structure with dimensions of $a = 0.476$ nm and $c = 2.562$ nm. This aligns with the crystallography of the Mo_6Co_7 type (Fig. 4(c)). The analysis from TEM-EDS indicates a high concentration of elements such as Mo, W, Nb, and Co, which matches the μ phase that was discovered in a referenced study [34]. In addition, the needle-like phase (marked by green arrows) precipitated at 1050°C (Figs. 3(c) and 4(d)), which is rich in Cr, Mo, and W, while the elemental contents of Cr, Mo, and W are lower than those in μ-phase (Table 2), corresponding to σ phase as found in references [35–36].

As the annealing temperature increases to 1150°C (Fig. 3(d)), the volume fraction of the (γ + γ′) eutectic phase decreased, and the Laves phase and the white granular μ phase were eliminated, but the morphology of the angular

phase has not changed. The selected area diffraction patterns analysis, represented in Fig. 4(d), reveals that the angular particles possess a face-centered cubic structure with approximate measurements of a lattice constant a = 0.424 nm and a crystal plane spacing d = 0.2223 nm. The TEM-EDS analysis displays that the atomic proportion of C is roughly equivalent to that of (Nb + Ti) in the angular phase, suggesting it is an MC carbide [9,37]. By analyzing the diffraction patterns, the orientation relationship between the γ′ phase and MC-type carbide can be determined as $\{\bar{1}\bar{1}1\}_{MC}\|\{1\bar{1}\bar{1}\}_{\gamma}$ with $\{112\}_{MC}\|\{112\}_{\gamma'}$ [38], seen from Fig. 4.

During the annealing treatment, the Laves phase and μ phase changed considerably. Fig. 5(a) shows the high-magnification morphologies of the μ-phase by SEM. One can observe that the structure of the μ-phase is mainly divided into blocky, needle-like, and rod-like, and the size is about 1–3 μm. The TEM-mapping image shows that the μ-phase is rich in Mo, Cr, Co, and Nb (Fig. 5(b) and (c)), which is consistent with Laves phase in elemental composition. For μ-phase, the atomic ratio satisfied the Mo_6Co_7 ratio, and the morphology exhibits more fineness. From Fig. 5(d), we can see that the composition of elements like Nb, Co, and Cr in the μ-phase is lower than that in the Laves phase; additionally, compared to the other two morphologies, the blocky μ-phase almost has the highest elemental content of Nb and Mo.

The μ-phase is generally formed during long-term aging. However, in this study, the μ-phase was produced after annealing treatment at 950°C for 8 h. It was found by the above analysis that there seems to be a relationship between the μ phase and the Laves phase. To further characterize the relationship between the μ and Laves phases, we used XRD to characterize the formation mechanism of μ phase, and the results are shown in Fig. 6. After the annealing temperature from 950 to 1050°C, the diffraction intensity of μ phase was increased and the diffraction intensity of Laves phase was weakened. Until the annealing temperature was 1150°C, the diffraction of the μ phase disappeared together with the Laves phase, indicating that the transformation of the precipitated during the annealing process (Laves → μ), this is consistent with the observation of electron microscopy, seen from Fig. 3. Moreover, the area portions of the intermetallic phases within the interdendritic regions are depicted in Fig. 6(b). One can observe that both Laves phase (3.9%–0.2%) and (γ + γ′) eutectic (9.8%–2.4%) decrease greatly with the increase of temperature from 0 to 1150°C. The amount of MC phase (4.1%–3.9%) does not change obviously at different annealing treatment temperatures. The μ phase (0–1.2%) increases greatly with the increase of temperature from 0 to 1050°C, but almost disappears at 1150°C.

Based on the equilibrium phase diagram generated by utilizing Thermo-Calc software, other equilibrium precipitates such as γ′, σ, μ, $M_{23}C_6$, Ni_5Zr, and M_2B were precipitated in the solid phase, from Fig. 7. Fig. 6(a) suggests that the uptick in the μ phase coincides with a reduction in the Laves phase. Nevertheless, the (γ + γ′) eutectic phase and Laves phase structure were not calculated through the equilibrium solidification model in Thermo-calc. This is dependent on the equilibrium phase determined by the lowest Gibbs energy in the program of the equilibrium solidification model. In the Scheil model, the computation of phases is based on non-equilibrium conditions corrected by segregation coefficients

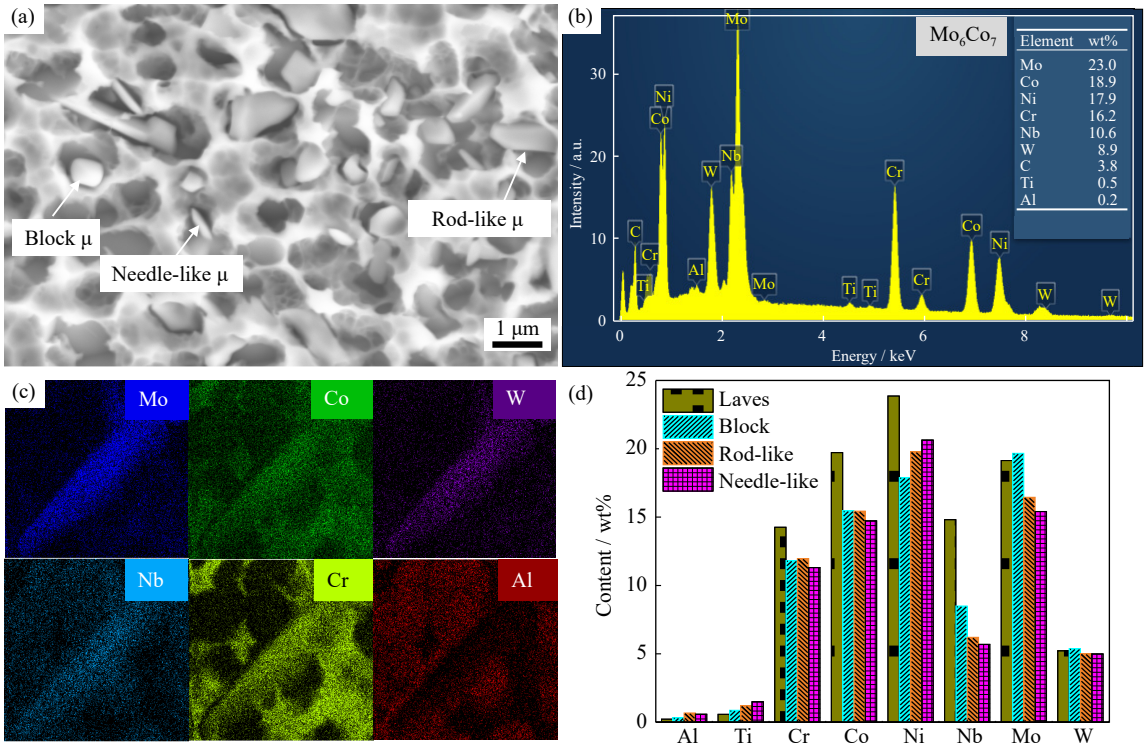

Fig. 5. (a) Morphologies and (b) composition of μ-phase obtained by the SEM-EDS and (c) TEM-mapping; (d) elemental contents in μ-phase and Laves phase.

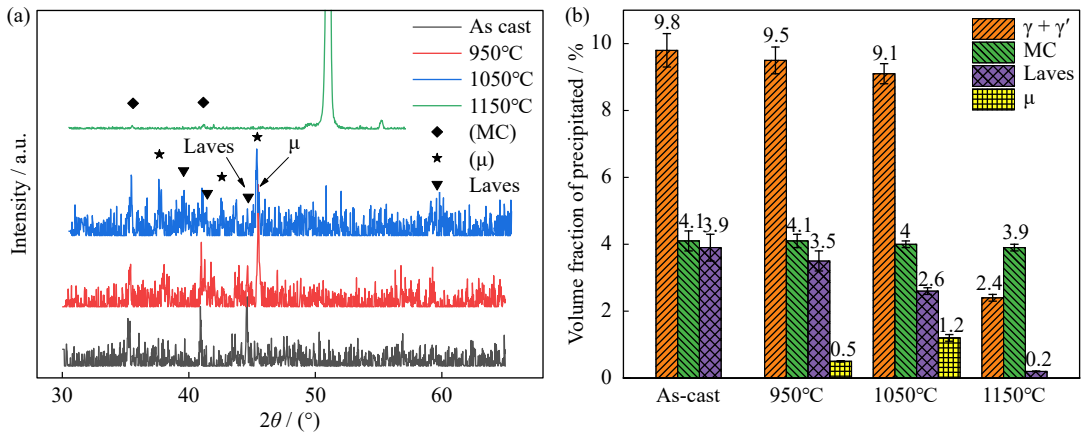

Fig. 6. (a) Typical XRD patterns of as-cast sample and annealed samples; (b) analysis of precipitated phases at different annealing temperatures.

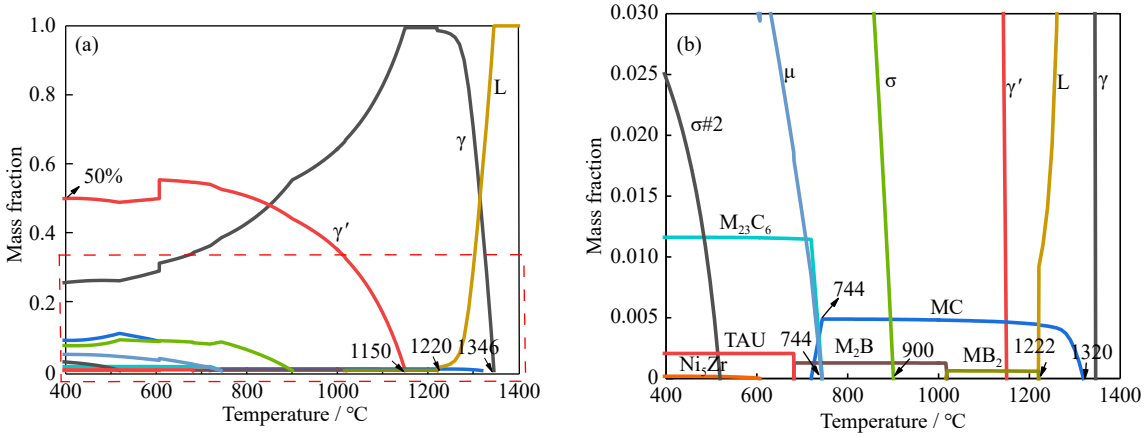

Fig. 7. (a) Relationship between the amount of equilibrium phase and the temperature; (b) partial magnification.

[39]. In addition, as shown in Fig. 7(b), the critical dissolving temperature of the μ phase is 744°C, which is lower than 950°C because the former is based on the solid phase precipitation in the equilibrium matrix, while the latter is obtained from the decomposition of Laves phase under experimental conditions.

Fig. 8 presents the bright-field image from TEM, along with the diffraction pattern taken from chosen segments of the square-shaped γ′ phase. The size of the large square γ'_{I} phase is 500–1000 nm, and the size of the secondary γ'_{II} is only 10–20 nm. The γ′ phase has a cube-on-cube orientation relationship with a lattice constant $a \approx 0.4083$ nm and a crystal plane spacing of $d = 0.245$ nm. As observed in Fig. 8(d), there's a single type of pattern for both the γ and γ′ phases. This is due to the overlapping of the diffraction patterns of the γ and γ′ phases, resulting from their fully coherent crystal relationship [40]. Besides, greater amounts of Al, Ti, Nb, and Ni were found concentrated in the γ′ phase, while elevated levels of Cr and Co were detected in the γ phase, from Fig. 8(e).

Fig. 9 shows the morphological characteristics of the γ′ phase after annealing treatment at different temperatures. Due to the uneven distribution of γ′-phase forming elements (Al, Ti) between interdendritic and dendrites in the conventional casting process, the size of γ′-phase in the interdendritic is larger than that of dendrites, and the average size of γ′-phase in the interdendritic is 1.0 μm (Fig. 9(a)), which is similar to the size of γ′-phase (0.86–4.14 μm) observed in the related literature [41]. The γ′ phase is L12 type structure $Ni_3(Al, Ti)$. With the increase of annealing temperature to 950°C (Fig. 9(b)) and 1050°C (Fig. 9(c)), the thermal activation energy of Al and Ti atoms in the supersaturated γ′ phase has heightened, thereby boosting the diffusion coefficient of Al and Ti. Consequently, this accelerates the precipitation and development of the γ′ phase. During annealing treatment at 950 and 1050°C, the morphological and average size of γ′-phase in the interdendritic is rod shape of (1.8 ± 0.5) μm and plum blossom shape of (2 ± 0.5) μm, respectively. However, when the temperature reaches the complete solid solution temperature of 1150°C (Fig. 9(d)), the γ′ phase coarsens in the opposite direction during the slow cooling rate (0.3°C/min), and the γ′-phase in the interdendritic is square shape of (2.5 ± 0.5) μm.

3.3. Mechanical properties

The tensile properties of the as-cast and annealing treatment samples tested at 800°C are shown in Fig. 10(a). GH4151 alloy is a precipitation-strengthened alloy, there is a strong interaction between strengthening phase γ′ and carbides, which strengthens the alloy by impeding disloca-

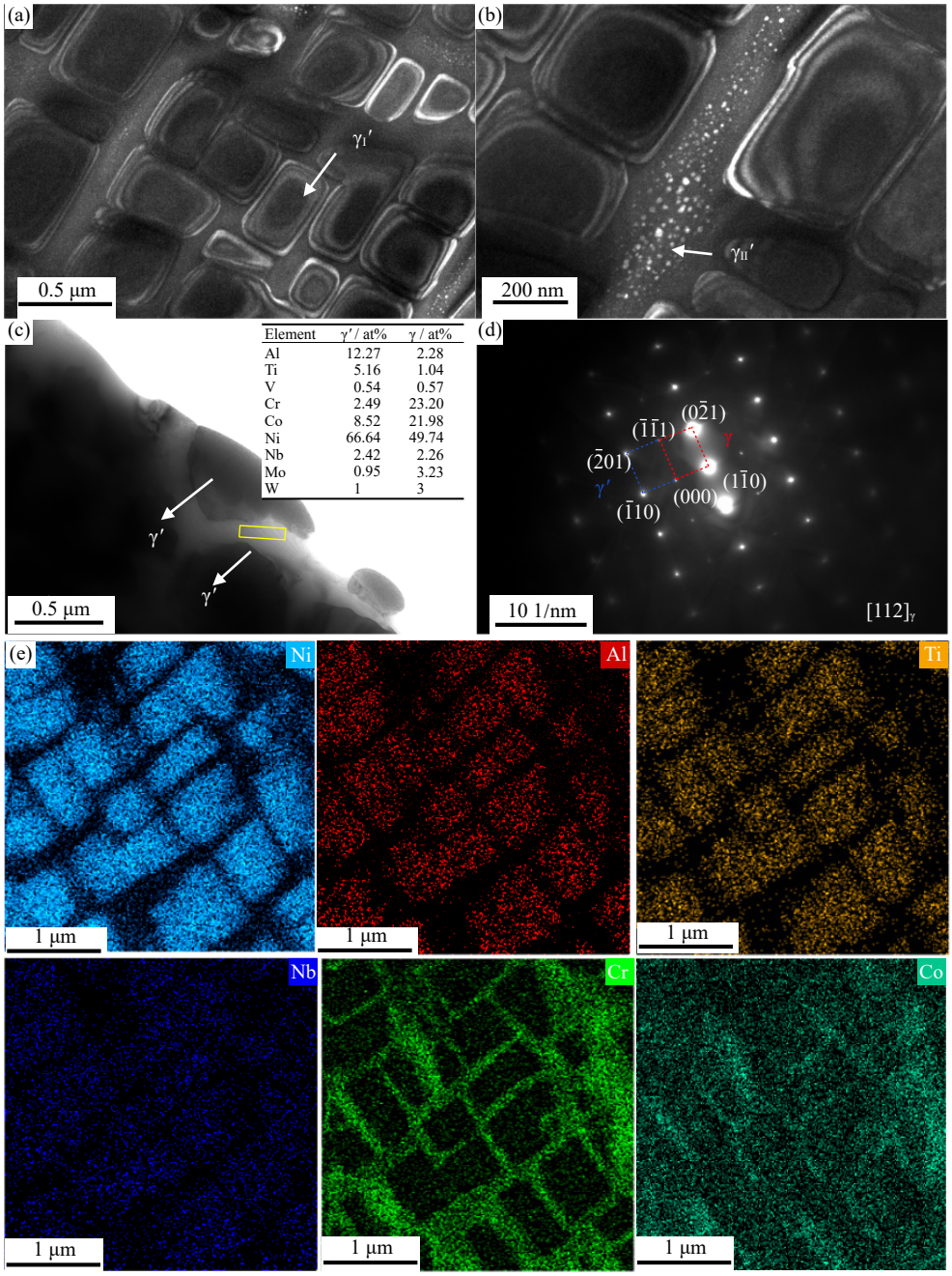

Fig. 8. (a–c) Bright field images, (d) selected area diffraction patterns, and (e) TEM-EDS of γ′.

tion movement. At the as-cast alloy (Fig. 10(b)), the grains are coarse, and large (γ + γ′) eutectic and Laves phases precipitated along the grain boundaries. Concurrently, the γ′ strengthening phase is large with small spacing, and the dislocations are difficult to pass, resulting in low strength and plasticity of the alloy (1060 MPa, 26.6%). Upon ramping up the annealing temperature to 950 and 1050°C (as shown in Fig. 10(b)), precipitation of the μ phase begins as the brittle Laves phase and the (γ + γ′) eutectic phase break down. Concurrently, as the γ′ phase gradually grows, both the strength and ductility of the matrix alloy increase, for instance, 1082 MPa, 27.7% and 1128 MPa, 37.4%. Nonetheless, when the annealing temperature is further escalated to 1150°C (also depicted in Fig. 10(b)), both the brittle Laves phase and μ phase are eradicated. Subsequently, the large-sized γ′ phase re-precipitates following the solid solution, and the alloy's strength–plasticity reaches its peak at 1394 MPa, 56.1%, which is a significant 131% and 200% increase compared to the as-cast alloy's strength–plasticity (1060 MPa, 26.6%).

The tensile characteristics of the annealed and as-cast samples evaluated at 25°C are illustrated in Fig. 10(c). The figure reveals a decrease in yield strength and an increase in plasticity due to the annealing process, largely attributed to the removal of the Laves phase [42] and expansion of the γ′ phase [11]. It's crucial to note that the alloy's tensile strength and plasticity show noticeable improvements when annealed at 950°C, compared to both the as-cast version and the one annealed at 1050°C. The impact of the μ-phase on the alloy is intricate and has not been fully comprehended to date. First of all, the fine μ-phase can play the role of second-phase

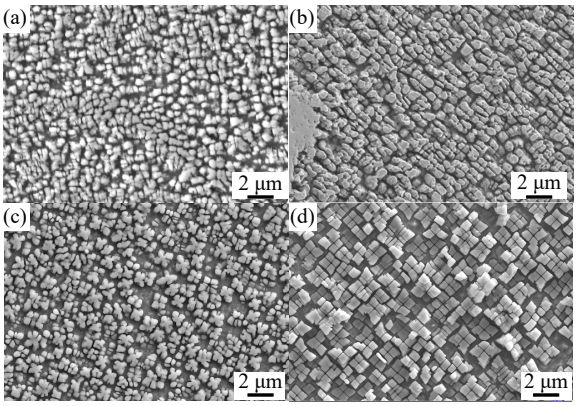

Fig. 9. γ′ phase morphologies of the (a) as-cast sample and annealed samples at different temperatures: (b) 950, (c) 1050, and (d) 1150°C.

strengthening and improve the strength of the alloy. However, the significant accumulation of μ-phase at 1050°C diminishes the presence of the solid solution strengthening component Mo within the matrix, thus reducing the strength of the alloy. Fig. 10(d) shows the instantaneous work hardening rate ($d\sigma/d\varepsilon$)–true strain curves, where the work hardening behaviors depict typical "three stages" hardening characteristics. In the first stage, the work hardening decreases rapidly with the increase of plastic strain. In the second stage, with the increase of strain, the work hardening rate increases rapidly, where the strain rate is maximum after annealing at 1150°C. In the third phase, a decline in the curve occurs as a result of dynamic recovery following an adequate accumulation of dislocations. The most rapid decline was noted at 1150°C.

3.4. Fracture morphology

Fig. 11 shows the cross-sectional and fracture morphology of the cracks under different annealing temperatures. It can be found that the as-cast alloy shows the porosity and (γ + γ′) eutectic phases in the cross-section, and with shallow dimples of varying sizes on the fracture surfaces. Annealing treatment leads to an increase in the plasticity of the alloy and results in an increase in the size of the dimples. With annealing temperature increased to 950 and 1050°C (Fig. 11(b) and (c)), the crack still occurs near the precipitated phase, but the size of the dimples increases. Moreover, the white μ phase forms, which hinders dislocation movement and improves the strength of grain boundaries. With a further increase in temperature to 1150°C (Fig. 11(d)), the brittle Laves and μ phases in the alloy were redissolved and only the MC phase was present; hence, the alloy's strength and plasticity were improved. Significantly, the fracture surface exhibits a distinct stress extension stripe and numerous densely packed short tear edges spread across. This can be observed in Fig. 11(h), which suggests that the alloy's fracture method is

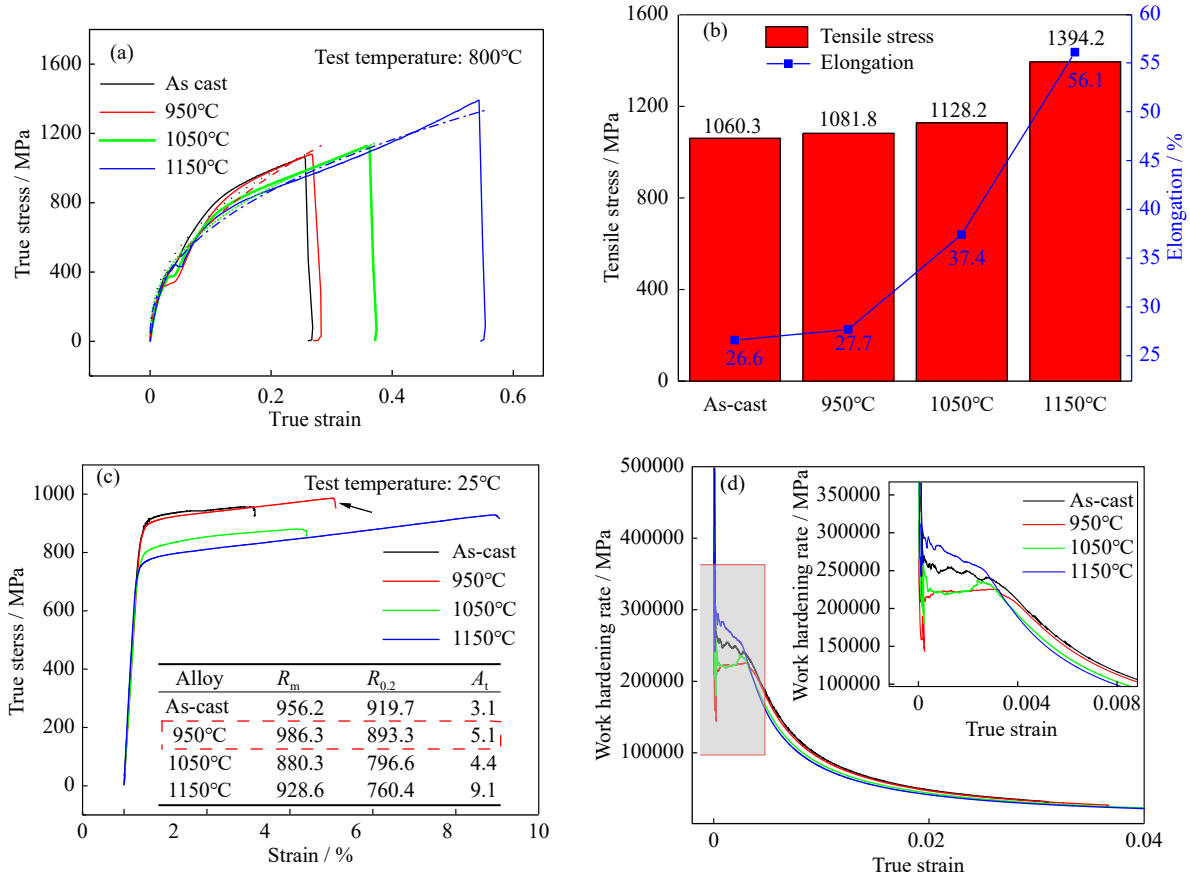

Fig. 10. Stress–strain curves of the GH4151 alloy annealed at different temperatures: (a) stress–strain tested at 800°C; (b) tensile strength and elongation; (c) stress–strain tested at 25°C (R_m—Tensile strength; $R_{0.2}$—Yield strength; A_t—Elongation); (d) work-hardening rate calculated based on room temperature stretching.

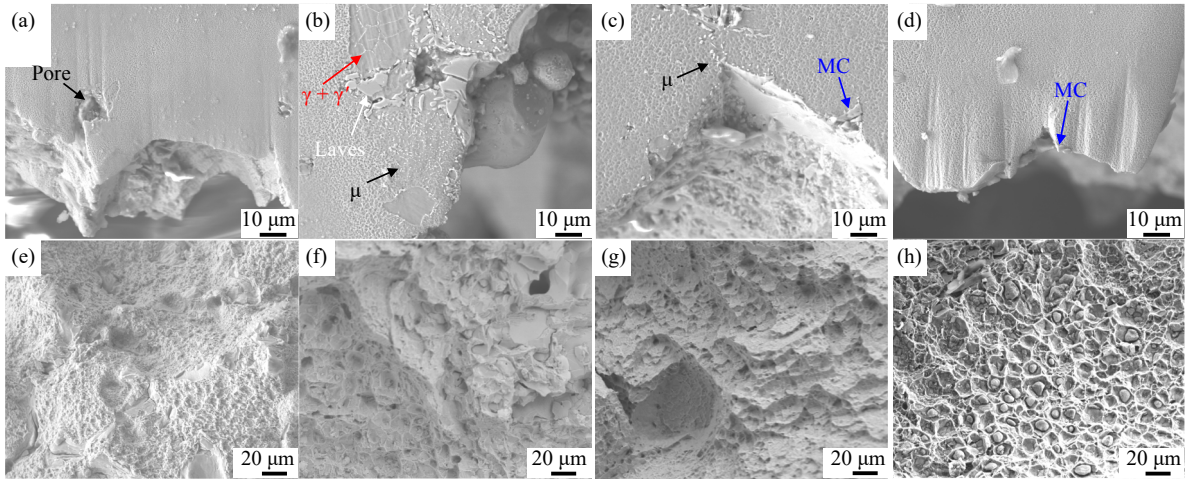

Fig. 11. Cross-sectional and fracture morphology of the GH4151 alloy annealed at different temperatures: (a, e) as-cast, (b, f) 950°C, (c, g) 1050°C, and (d, h) 1150°C.

typical of quasi cleavage-fracture.

Furthermore, upon raising the annealing temperature to 1150°C, spherical La–Ni–O phases could be seen on the fracture surface as presented in Fig. 11(h) and Fig. 12. Conversely, at an annealing temperature of 1050°C, the overall oxidation is not reduced due to absent aggregated oxides (La–O oxides) from the large La–Ni phases [43]. According to Song and colleagues [44], it was found that when these alloys undergo oxidation at 1100°C, the La–Ni intermetallic phases become unstable and oxidize into La–O oxides, thereby speeding up the oxidation reaction. However, $LaCrO_3$ formed at a medium temperature of 1000°C can reduce the growth rate of Cr-oxide by inhibiting Cr^{3+} diffusion and enhancing the oxidation resistance of the alloy [45]. In summary, the alloy with annealing temperature of 1150°C has high strength and plasticity (1394 MPa, 56.1%), but the oxidation process in the alloy is accelerated, while the oxidation rate is lower when annealing is performed at 1050°C and the plasticity and strength of the alloy is 1128 MPa and 37.4%, from Fig. 10(b).

3.5. Microstructure evolution

Local strain levels and brittle precipitates are demonstrated as critical factors for the cracking of superalloys [46–47]. If the remaining stress exceeds the alloy's tensile strength, cracking is bound to happen [11]. Residual stress acts similarly to an additional burden on a component, which originates from both thermal stress stemming from variances in temperature and structural stress generated by the processes of precipitation and segregation [3]. Stress-relieving

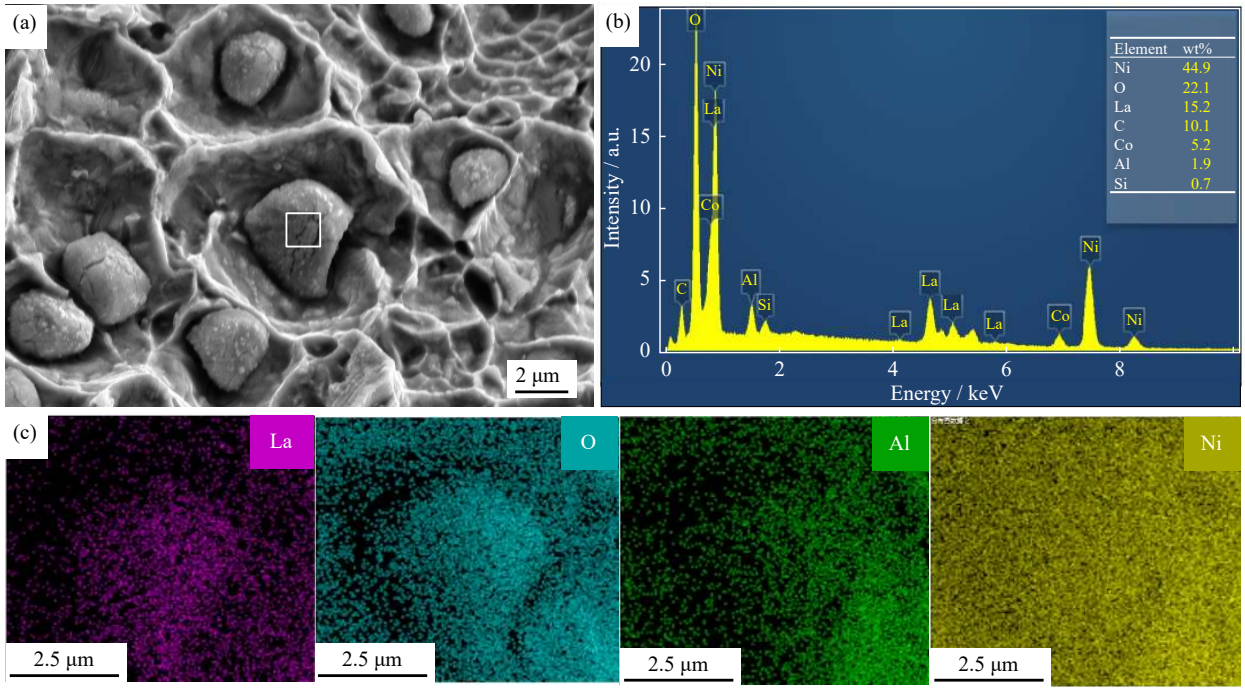

Fig. 12. (a) Ni–La–O phase observed on the fracture surface of tensile specimens annealed at 1150°C; (b) EDS of the Ni–La–O phase; (c) EDS-mapping of the Ni–La–O phase.

annealing can prove the presence of residual stresses [48]. Fig. 13 shows the recrystallization distribution of EBSD. The blue area is the recrystallized grain, the yellow area is the unfinished recrystallized substructure, and the red area is the original tissue without recrystallization. The dynamically recrystallized grains occur in the as-cast alloy under the influence of thermal stresses in the cold-casting mold during the VIM progress, from Fig. 13(a). Combined with the results of recrystallization ratio statistics (Fig. 13(e)), it can be seen that a rise in annealing temperature leads to a gradual increase in recrystallization ratio and a significant static recrystallization behavior.

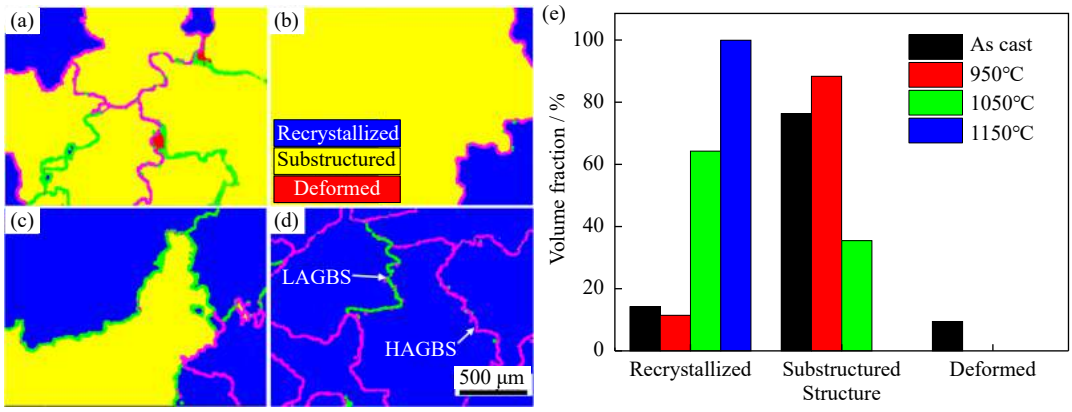

Fig. 13. Recrystallization distribution of (a) as-cast sample and annealed samples at different temperatures: (b) 950, (c) 1050, and (d) 1150°C; (e) recrystallization ratio.

The VIM melting process is due to a small temperature gradient and slow cooling rate (temperature gradient V: ~10^{-1}–10^{-2}°C·mm^{-1} and cooling rate G: ~1–10°C·s^{-1}), resulting in a relatively small number of grains forming, with the grains growing fully. The average grain size of the GH4151 alloy is 0.5–2 mm. Fig. 14 reveals the pattern of dislocation for both the as-cast and annealing treatments at varying temperatures. Regarding the as-cast alloy (seen in Fig. 14(a)), the dislocation was hindered by γ′ phase, resulting in entanglement and plugging. GH4151 alloy belongs to a low stacking fault (SFE) energies Ni-based superalloys, in which the extended dislocations are difficult to gather, cross-slip, and climb. After annealing at 950°C (Fig. 14(b)), the dislocation density around the γ′ phase was significantly reduced in most areas, but in a few regions, the dislocation tangled and formed a cellular structure. When the annealing temperature was increased to 1050°C (Fig. 14(c)), the dislocations in the cellular structure were absorbed, and the dislocations shear the γ′ phase and migrate to the subgrain boundary. As the annealing temperature rose to 1150°C (Fig. 14(d)), the dislocations are plugged, traversed, and annihilated at the grain boundaries, leading to an increase in the misorientation, which changes the grain boundary angle and transforms the grain boundary type.

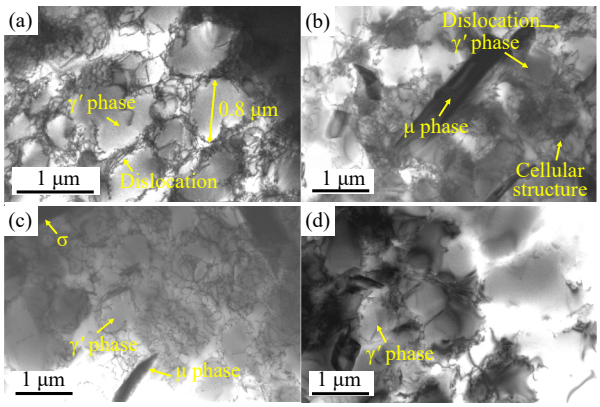

Fig. 14. Dislocation distribution in the (a) as-cast sample and annealed sample at different temperatures: (b) 950, (c) 1050, and (d) 1150°C.

3.6. Residual stress

To quantitatively reflect the residual stress in the material, it was calculated by the Kubin and Mortensen formula (3):

$$\rho_{gnd} = \frac{2\theta_{KAM}}{d\boldsymbol{b}} \tag{3}$$

where ρ_{gnd} and θ_{KAM} are the geometric dislocation density and kernel average misorientation, respectively; $\boldsymbol{b}$ = 2.5 × 10^{-10} m is the Burgers vector [49] and d = 6.5 μm is the unit step of the selected point. From the equation, it can be seen that with the increase of kernel average misorientation θ_{KAM}, indicating the higher the residual stress in the alloy. As shown in Fig. 15(a), the local orientation difference θ_{KAM} is concentrated in 0°–1.5°, and the distribution is less in 1.5°–5°. With increasing annealing temperatures at 950, 1050, and 1150°C, the kernel average misorientation θ_{KAM} shifts significantly to the left, and the peaks of the θ_{KAM} are 0.35°, 0.25°, 0.15°, respectively. In summary, the peak of θ_{KAM} left shift indicating that the residual stress of the alloy is released. Fig. 15(b) shows the residual stress and microhardness of as-cast and annealed samples. Among them, the residual stress and microhardness in the as-cast sample were 60.1 MPa and HV 423, and after annealing at 1150°C, the residual stress and microhardness were significantly reduced to 10.9 MPa and HV 323. It can be understood that the sufficient precipitation of the γ′ phase reduces the solute atoms in the matrix, thus weakening the solid solution strengthening in the matrix and reducing the hardness of the alloy.

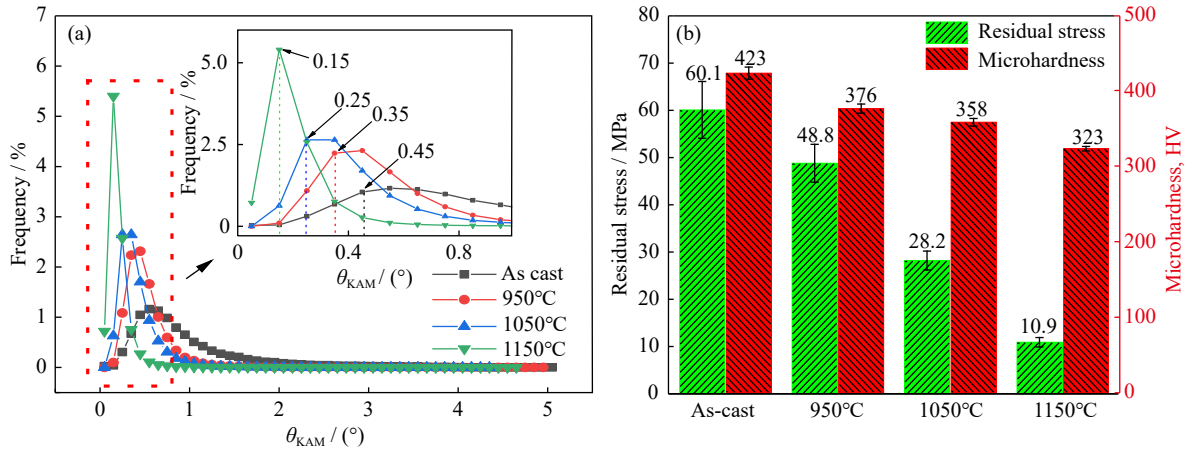

Fig. 15. (a) Distribution curves of local misorientation of as-cast and annealed samples; (b) residual stress and microhardness of as-cast and annealed samples.

4. Discussion

4.1. Microstructure evolution of the annealing process

Based on the thermodynamic principle of thermal expansion and contraction, the alloy liquid falls into the cast iron mold, and the alloy liquid is confined by the solidified part to produce compressive stress. In addition, influenced by the thermal stresses generated during solidification and the structural stresses generated by the precipitation of the γ′ phase, a large number of dislocations accumulated in the material. After the stress relief annealing treatment, the alloy undergoes stages of reversion, recrystallization, and grain growth during the annealing process. When the annealing temperature is 950 or 1050°C, the effect of thermal activation leading to the rearrangement of dislocations is smaller, and the hindering effect of dislocation movement is dominant, which is manifested as dislocation strengthening. By further increasing the annealing temperature to 1150°C, the dislocations rearrange and move inside the crystal, and the different numbers of dislocations counteract each other, resulting in the disappearance of a large number of dislocations. However, due to the elimination of Laves phase and μ phase and precipitation of a large size γ′ phase during the annealing process at 1150°C, the strength of the alloy increases as a precipitation phase strengthens. With the substantial reduction of dislocation density, the residual stress of the material also decreases, and θ_{KAM} gradually decreases. The mechanism of stress relaxation involves the interplay of dislocation slip and the migration of grain boundaries.

4.2. Precipitation evolution at the annealing process

Introducing high quantities of alloying components can cause substantial element segregation as the alloy solidifies, leading to an irregular dispersion of the rough (γ + γ′) phase, the Laves phase, and the angular MC carbide [50]. With the increase of annealing temperature, the thermal activation energy for Al and Ti atoms in the supersaturated matrix and Cr, Mo, Nb, and Co in the Laves phase is increased, and the diffusion coefficient is larger and easier to migrate, thus promoting the growth of the γ′ phase and the decomposition of the Laves phase. When the temperature reaches 950°C, fine-grained μ-phase forms around the grain boundaries and Laves phase. The white granular μ phase becomes more obvious when the temperature is further increased to 1050°C. As the temperature increases to 1150°C, the Laves phase and the white granular μ phase are eliminated and the volume fraction of the (γ + γ′) eutectic phase decreases. This can be understood as the homogenization process of the precipitated phases in the alloy. From the analysis of the evolution of the precipitated phases and the composition of μ and Laves phases and MC carbide, it is assumed that the main constituents of Laves-phase and μ-phase are Mo and Nb, which are also the main components of MC carbide, and therefore the formation of MC carbide will be promoted during the resolution process. This can be interpreted as controlling the distribution of the MC carbide by controlling the segregation of Laves phase.

4.3. Effect of the annealing process on mechanical properties

As a precipitation-hardened superalloy, the yield strength (σ_{YS}) of the GH4151 alloy is primarily derived from the inherent strength (σ_0) of unadulterated nickel, enhancement at the grain boundaries ($\Delta\sigma_D$), the solid solution fortification of γ matrix ($\Delta\sigma_{ss}$), dislocation reinforcement ($\Delta\sigma_b$), and precipitation amplification ($\Delta\sigma_p$).

$$\sigma_{YS} = \sigma_0 + \Delta\sigma_D + \Delta\sigma_{ss} + \Delta\sigma_b + \Delta\sigma_p \quad (4)$$

The inherent strength (σ_0) can be represented by a specific formula $\sigma_0 = M \cdot \tau_{crss}$, where $M = 2.5$, which is the Taylor factor, and $\tau_{crss} = 17.5$ MPa, known as the critical resolved shear stress for Ni-based superalloy [42]. Moreover, the role of grain boundary fortification in contributing to the yield strength is typically outlined using the Hall-Petch equation $\sigma_D = \frac{\kappa}{D^{1/2}}$ [42], where $D = 650$ μm, the grain size measured via EBSD as shown in Fig. 9, and the Hall-Petch coefficient κ is 750 MPa·μm$^{1/2}$ in Ni-based superalloy [51]. Additionally, the function of the solid-solution strengthening can be described by $\Delta\sigma_{ss} = [\sum_i (a_i^2 \cdot c_i)]^{1/2}$ [52], where a_i signifies the constant of the solute atom's fortification, as seen in

Table 3, and c_i denotes the solute atom's content, as shown in Fig. 8(c).

Table 3. Strengthening constant of solute atoms in nickel [52]
(MPa·at%$^{-1}$)

a_{Al}	a_{Ti}	a_{Cr}	a_{Co}	a_{Nb}	a_{Mo}	a_W	a_V
225	775	337	520	1183	1015	977	408

Moreover, the increase in strength due to dislocation hardening ($\Delta\sigma_b$) can be outlined as follows, $\Delta\sigma_b = M\alpha G_m \boldsymbol{b}\rho_{total}^{\frac{1}{2}}$ [53], where $M = 2.5$, which is the Taylor factor, $\alpha = 0.2$ for high dislocation density, the shear modulus of the matrix $G_m = 76$ GPa [54], and $\boldsymbol{b} = 0.25$ nm is the Burgers vector. The value of ρ_{total} is the dislocations density $\rho_{GNDs} = 1.82\times10^{14}$ m^{-2} at 1150°C. The increase in intensity from precipitation hardening ($\Delta\sigma_p$) can be credited to the bypass of Orowan precipitates and the shearing process as dislocations shear across precipitates. Here, the γ′ phase size $R = 1.77$ μm far exceeds the critical size $R = 26$ nm reported by Zhang *et al.* [55]. Therefore, the Orowan mechanism strengthening ($\Delta\sigma_{\gamma'}$) can be considered [28].

$$\Delta\sigma_{\gamma'\text{-Orowan(spheres)}} = \frac{0.85MG\boldsymbol{b}}{2\pi(1-\nu)^{1/2}}\frac{1}{2R\left[\sqrt{\left(\frac{\pi}{6f}\right)}-\sqrt{\frac{2}{3}}\right]}\ln\left(\frac{2\sqrt{\frac{2}{3}}R}{r_0}\right) \quad (5)$$

In this case, $M = 2.5$, is the Taylor factor. The shear modulus of the matrix, represented by $G = 76$ GPa. The Burgers vector, denoted by $\boldsymbol{b} = 0.25$ nm, and the Poisson ratio is $\nu = 0.3$. The dislocation core radius, $r_0 = 0.25$ nm. The volume fraction of the strengthening phases $f = 50\%$. Considering the 2.5-μm square γ′ phase to be spherical in shape, the radius of the spherical γ′ phase, $R = 1.77$ μm.

The influence of the pretreatment process on the strength of GH4151 annealed at 1150°C alloy is mainly derived from the solid solution strengthening of γ matrix ($\Delta\sigma_{ss}$), seen from Table 4. In addition, the contribution of MC phase and residual (γ + γ′) eutectic relative to strength is not considered, which may be the main reason why the calculated yield strength (σ_{YS}) value is smaller than the experimental strength ($\sigma_{Experimental}$).

Table 4. Strength contributions of various strengthening mechanisms for alloy annealed at 1150°C MPa

σ_0	$\Delta\sigma_D$	$\Delta\sigma_{ss}$	$\Delta\sigma_b$	$\Delta\sigma_{\gamma'}$	σ_{YS}	$\sigma_{Experimental}$
43.75	29.42	431.88	128.04	88.22	721.33	760.43

5. Conclusions

In this paper, the effects of stress relieving annealing treatment on the microstructure, residual stresses, precipitation, and mechanical properties of GH4151 alloy, and the main conclusions are as follows:

(1) After the stress relief annealing treatment of GH4151 alloy at different temperatures (950–1150°C), the dislocation migration rearranged, leading to the transition from low-angle grain boundaries to high-angle grain boundaries. In addition, the local orientation difference gradually decreases (0.45°–0.15°), and the mechanism of structural evolution is static recrystallization. Most of the residual stresses were released from 60.1 to 10.9 MPa.

(2) During the annealing treatment at different temperatures, the primary γ′ phase precipitated from spherical (as cast for (1 ± 0.3) μm) and grew gradually to form a short rod-shaped γ′ phase (950°C for (1.8 ± 0.5) μm), plume-shaped γ′ phase (1050°C for (2 ± 0.5) μm), and square shape γ′ phase (1150°C for (2.5 ± 0.5) μm). Moreover, with the gradual decomposition of the Laves-(Mo, Cr, Co, Nb) phase, the μ-(Mo_6Co_7) phase began to precipitate, and a large amount of white granular μ phase precipitated at 1050°C until the elimination of μ phase and Laves phase at 1150°C.

(3) During the annealing treatment at different temperatures, the VIM GH4151 alloy shows an increase in strength and plasticity and a decrease in hardness compared to the as-cast. When the annealing temperature is increased to 1150°C, the strength plasticity of the alloy reached the maximum and microhardness reached the minimum (1394 MPa, 56.1%, HV 323), which were 131%, 200%, and 76% fold than those of the as-cast alloy (1060 MPa, 26.6%, HV 423), but the oxidation process in the alloy is accelerated at 1150°C.

Acknowledgements

This work was financially supported by the National Science and Technology Major Project of China (No. J2019-VI-0006-0120), the National Key R&D Program of China (No. 2021YFB3700402), and the National Natural Science Foundation of China (Nos. 52074092 and 52274330).

Conflict of Interest

My co-authors and I would like to have this statement that the paper is original, which has not been submitted elsewhere for publication, in whole or in part, and we declare that we do not have any commercial or associative interest that represents a conflict of interest in connection with the work submitted.

References

[1] E. Chlebus, K. Gruber, B. Kuźnicka, J. Kurzac, and T. Kurzynowski, Effect of heat treatment on the microstructure and mechanical properties of Inconel 718 processed by selective laser melting, *Mater. Sci. Eng. A*, 639(2015), p. 647.

[2] G.D. Zhao, X.M. Zang, Y. Jing, N. Lü, and J.J. Wu, Role of carbides on hot deformation behavior and dynamic recrystallization of hard-deformed superalloy U720Li, *Mater. Sci. Eng. A*, 815(2021), art. No. 141293.

[3] M.C. Hardy, M. Detrois, E.T. McDevitt, *et al.*, Solving recent challenges for wrought Ni-base superalloys, *Metall. Mater. Trans. A*, 51(2020), No. 6, p. 2626.

[4] Y.X. Zhu, C. Li, Y.C. Liu, Z.Q. Ma, and H.Y. Yu, Effect of Ti addition on high-temperature oxidation behavior of Co–Ni-based superalloy, *J. Iron Steel Res. Int.*, 27(2020), No. 10, p. 1179.
[5] S.L. Yang, S.F. Yang, W. Liu, J.S. Li, J.G. Gao, and Y. Wang, Microstructure, segregation and precipitate evolution in directionally solidified GH4742 superalloy, *Int. J. Miner. Metall. Mater.*, 30(2023), No. 5, p. 939.
[6] S.M. Lv, J.B. Chen, X.B. He, C.L. Jia, K. Wei, and X.H. Qu, Investigation on sub-solvus recrystallization mechanisms in an advanced γ–γ′ nickel-based superalloy GH4151, *Materials*, 13(2020), No. 20, art. No. 4553.
[7] L. Jia, H. Cui, S.F. Yang, S.M. Lv, X.F. Xie, and J.L. Qu, Effect of carbon addition on microstructure and mechanical properties of a typical hard-to-deform Ni-base superalloy, *Prog. Nat. Sci. Mater. Int.*, 33(2023), No. 2, p. 232.
[8] X.X. Li, C.L. Jia, Y. Zhang, S.M. Lv, and Z.H. Jiang, Segregation and homogenization for a new nickel-based superalloy, *Vacuum*, 177(2020), art. No. 109379.
[9] Y.G. Tan, F. Liu, A.W. Zhang, *et al*., Element segregation and solidification behavior of a Nb, Ti, Al co-strengthened superalloy ЭК151, *Acta Metall. Sin. Engl. Lett.*, 32(2019), No. 10, p. 1298.
[10] M.M. Bakradze, S.V. Ovsepyan, A.A. Buiakina, and B.S. Lomberg, Development of Ni-base superalloy with operating temperature up to 800°C for gas turbine disks, *Inorg. Mater. Appl. Res.*, 9(2018), No. 6, p. 1044.
[11] X.X. Li, C.L. Jia, Y. Zhang, S.M. Lü, and Z.H. Jiang, Cracking mechanism in as-cast GH4151 superalloy ingot with high γ′ phase content, *Trans. Nonferrous Met. Soc. China*, 30(2020), No. 10, p. 2697.
[12] M.H. Zhang, B.C. Zhang, Y.J. Wen, and X.H. Qu, Research progress on selective laser melting processing for nickel-based superalloy, *Int. J. Miner. Metall. Mater.*, 29(2022), No. 3, p. 369.
[13] L. Zhang, L. Wang, Y. Liu, X. Song, T. Yu, and R. Duan, Hot cracking behavior of large size GH4742 superalloy vacuum induction melting ingot, *J. Iron Steel Res. Int.*, 29(2022), No. 9, p. 1505.
[14] F. D'Elia, C. Ravindran, and D. Sediako, Interplay among solidification, microstructure, residual strain and hot tearing in B206 aluminum alloy, *Mater. Sci. Eng. A*, 624(2015), p. 169.
[15] Y. Li, H.X. Li, L. Katgerman, Q. Du, J.S. Zhang, and L.Z. Zhuang, Recent advances in hot tearing during casting of aluminium alloys, *Prog. Mater. Sci.*, 117(2021), art. No. 100741.
[16] X.Q. Zhang, H.B. Chen, L.M. Xu, J.J. Xu, X.K. Ren, and X.Q. Chen, Cracking mechanism and susceptibility of laser melting deposited Inconel 738 superalloy, *Mater. Des.*, 183(2019), art. No. 108105.
[17] X.Z. Zhou, Y.H. Zhang, Y. Zhang, H.D. Fu, and J.X. Xie, Effect of Ni content on solidification behavior and hot-tearing susceptibility of Co–Ni–Al–W-based superalloys, *Metall. Mater. Trans. A*, 53(2022), No. 9, p. 3465.
[18] Y.S. Li, Y.W. Dong, Z.H. Jiang, *et al*., Study on microsegregation and homogenization process of a novel nickel-based wrought superalloy, *J. Mater. Res. Technol.*, 19(2022), p. 3366.
[19] Z. Zhao and J.X. Dong, Effect of eutectic characteristics on hot tearing of cast superalloys, *J. Mater. Eng. Perform.*, 28(2019), No. 8, p. 4707.
[20] X.X. Li, C.L. Jia, Z.H. Jiang, Y. Zhang, and S.M. Lv, Investigation of solidification behavior in a new high alloy Ni-based superalloy, *JOM*, 72(2020), No. 11, p. 4139.
[21] S. Kou, A criterion for cracking during solidification, *Acta Mater.*, 88(2015), p. 366.
[22] J.J. Xu, X. Lin, P.F. Guo, *et al*., The initiation and propagation mechanism of the overlapping zone cracking during laser solid forming of IN-738LC superalloy, *J. Alloys Compd.*, 749(2018), p. 859.
[23] M.D. Rowe, Ranking the resistance of wrought superalloys to strain-age cracking, *Welding J.*, 85(2006), No. 2, p. 27-s.
[24] J.P. Oliveira, A.D. LaLonde, and J. Ma, Processing parameters in laser powder bed fusion metal additive manufacturing, *Mater. Des.*, 193(2020), art. No. 108762.
[25] E. Edin, F. Svahn, M. Neikter, and P. Åkerfeldt, Stress relief heat treatment and mechanical properties of laser powder bed fusion built 21-6-9 stainless steel, *Mater. Sci. Eng. A*, 868(2023), art. No. 144742.
[26] B. Diepold, N. Vorlaufer, S. Neumeier, T. Gartner, and M. Göken, Optimization of the heat treatment of additively manufactured Ni-base superalloy IN718, *Int. J. Miner. Metall. Mater.*, 27(2020), No. 5, p. 640.
[27] Y.T. Ding, H. Wang, J.Y. Xu, Y. Hu, and D. Zhang, Evolution of microstructure and properties of SLM formed inconel 738 alloy during stress relief annealing, *Rare Met. Mater. Eng.*, 49(2020), No. 12, p. 4311.
[28] J.J. Zhu and W.H. Yuan, Effect of pretreatment process on microstructure and mechanical properties in Inconel 718 alloy, *J. Alloys Compd.*, 939(2023), art. No. 168707.
[29] H. Wang, X. Zhang, G.B. Wang, *et al*., Selective laser melting of the hard-to-weld IN738LC superalloy: Efforts to mitigate defects and the resultant microstructural and mechanical properties, *J. Alloys Compd.*, 807(2019), art. No. 151662.
[30] S. Carlsson and P.L. Larsson, On the determination of residual stress and strain fields by sharp indentation testing. Part I: Theoretical and numerical analysis, *Acta Mater.*, 49(2001), No. 12, p. 2179.
[31] C. Zhu, Z.H. Zhao, Q.F. Zhu, *et al*., Hot-top direct chill casting assisted by a twin-cooling field: Improving the ingot quality of a large-size 2024 Al alloy, *J. Mater. Sci. Technol.*, 112(2022), p. 114.
[32] G.D. Zhao, G.L. Yang, F. Liu, X. Xin, and W.R. Sun, Transformation mechanism of (γ+γ′) and the effect of cooling rate on the final solidification of U720Li alloy, *Acta Metall. Sin. Engl. Lett.*, 30(2017), No. 9, p. 887.
[33] X.X. Li, C.L. Jia, Y. Zhang, S.M. Lü, and Z.H. Jiang, Incipient melting phase and its dissolution kinetics for a new superalloy, *Trans. Nonferrous Met. Soc. China*, 30(2020), No. 8, p. 2107.
[34] H.M. Tawancy, Precipitation characteristics of μ-phase in wrought nickel-base alloys and its effect on their properties, *J. Mater. Sci.*, 31(1996), No. 15, p. 3929.
[35] W. Sun, X.Z. Qin, J.T. Guo, L.H. Lou, and L.Z. Zhou, Microstructure stability and mechanical properties of a new low cost hot-corrosion resistant Ni–Fe–Cr based superalloy during long-term thermal exposure, *Mater. Des.*, 69(2015), p. 70.
[36] A. Agh and A. Amini, Investigation of the stress rupture behavior of GTD-111 superalloy melted by VIM/VAR, *Int. J. Miner. Metall. Mater.*, 25(2018), No. 9, p. 1035.
[37] R. Liu, X.T. Wang, P.P. Hu, C.B. Xiao, and J.S. He, Low cycle fatigue behavior of micro-grain casting K4169 superalloy at room temperature, *Prog. Nat. Sci. Mater. Int.*, 32(2022), No. 6, p. 693.
[38] H. Xu, Y.H. Zhang, H.D. Fu, F. Xue, X.Z. Zhou, and J.X. Xie, Effects of boron or carbon on solidification behavior of Co–Ni–Al–W-based superalloys, *J. Alloys Compd.*, 891(2022), art. No. 161965.
[39] L. Gong, B. Chen, Z.H. Du, M.S. Zhang, R.C. Liu, and K. Liu, Investigation of solidification and segregation characteristics of cast Ni-base superalloy K417G, *J. Mater. Sci. Technol.*, 34(2018), No. 3, p. 541.
[40] Y.L. Xu, Q.M. Jin, X.S. Xiao, *et al*., Strengthening mechanisms of carbon in modified nickel-based superalloy Nimonic 80A, *Mater. Sci. Eng. A*, 528(2011), No. 13-14, p. 4600.
[41] X.L. Su, Q.Y. Xu, R.N. Wang, Z.L. Xu, S.Z. Liu, and B.C. Liu, Microstructural evolution and compositional homogenization of

a low re-bearing Ni-based single crystal superalloy during through progression of heat treatment, *Mater. Des.*, 141(2018), p. 296.
[42] S. Sui, H. Tan, J. Chen, *et al*., The influence of Laves phases on the room temperature tensile properties of Inconel 718 fabricated by powder feeding laser additive manufacturing, *Acta Mater.*, 164(2019), p. 413.
[43] M.Q. Ding, P. Hu, Y. Ru, *et al*., Effects of rare-earth elements on the oxidation behavior of γ-Ni in Ni-based single crystal superalloys: A first-principles study from a perspective of surface adsorption, *Appl. Surf. Sci.*, 547(2021), art. No. 149173.
[44] X. Song, L. Wang, Y. Liu, and H.P. Ma, Effects of temperature and rare earth content on oxidation resistance of Ni-based superalloy, *Prog. Nat. Sci. Mater. Int.*, 21(2011), No. 3, p. 227.
[45] H.M. Tawancy and N.M. Abbas, An analytical electron microscopy study of the role of La and Y during high-temperature oxidation of selected Ni-base alloys, *Scripta Metall. Mater.*, 29(1993), No. 5, p. 689.
[46] W.Z. Zhou, Y.S. Tian, Q.B. Tan, *et al*., Effect of carbon content on the microstructure, tensile properties and cracking susceptibility of IN738 superalloy processed by laser powder bed fusion, *Addit. Manuf.*, 58(2022), art. No. 103016.
[47] N.N. Lu, Z.L. Lei, K. Hu, *et al*., Hot cracking behavior and mechanism of a third-generation Ni-based single-crystal superalloy during directed energy deposition, *Addit. Manuf.*, 34(2020), art. No. 101228.
[48] E. Chauvet, P. Kontis, E.A. Jägle, *et al*., Hot cracking mechanism affecting a non-weldable Ni-based superalloy produced by selective electron Beam Melting, *Acta Mater.*, 142(2018), p. 82.
[49] T. Ungár, I. Dragomir, Révész, and A. Borbély, The contrast factors of dislocations in cubic crystals: The dislocation model of strain anisotropy in practice, *J. Appl. Crystallogr.*, 32(1999), No. 5, p. 992.
[50] B. Dubiel, P. Indyka, I. Kalemba-Rec, *et al*., The influence of high temperature annealing and creep on the microstructure and chemical element distribution in the γ, γ′ and TCP phases in single crystal Ni-base superalloy, *J. Alloys Compd.*, 731(2018), p. 693.
[51] R.W. Kozar, A. Suzuki, W.W. Milligan, J.J. Schirra, M.F. Savage, and T.M. Pollock, Strengthening mechanisms in polycrystalline multimodal nickel-base superalloys, *Metall. Mater. Trans. A*, 40(2009), No. 7, p. 1588.
[52] H.A. Roth, C.L. Davis, and R.C. Thomson, Modeling solid solution strengthening in nickel alloys, *Metall. Mater. Trans. A*, 28(1997), No. 6, p. 1329.
[53] J.S. Wang, M.D. Mulholland, G.B. Olson, and D.N. Seidman, Prediction of the yield strength of a secondary-hardening steel, *Acta Mater.*, 61(2013), No. 13, p. 4939.
[54] T.Q. Liu, Z.X. Cao, H. Wang, G.L. Wu, J.J. Jin, and W.Q. Cao, A new 2.4 GPa extra-high strength steel with good ductility and high toughness designed by synergistic strengthening of nanoparticles and high-density dislocations, *Scripta Mater.*, 178(2020), p. 285.
[55] S.Y. Zhang, X. Lin, L.L. Wang, *et al*., Strengthening mechanisms in selective laser-melted Inconel718 superalloy, *Mater. Sci. Eng. A*, 812(2021), art. No. 141145.